Optimization for maximizing the impact-resistance of patch repaired CFRP laminates using a surrogate-based model

Ying Tie, Yuliang Hou, Cheng Li, Liang Meng, Thaneshan Sapanathan, Mohamed Rachik

Version of Record: https://www.sciencedirect.com/science/article/pii/S0020740319340081
Manuscript_3e4b1752578d34a8a19921483f69e683

Optimization for maximizing the impact-resistance of patch repaired CFRP laminates using a surrogate-based model

Ying Tie[a], Yuliang Hou[a,b,*], Cheng Li[a], Liang Meng[b], Thaneshan Sapanathan[c], Mohamed Rachik[b]

[a] *School of Mechanical and Power Engineering, Zhengzhou University, Science Road 100, 450001, Zhengzhou,China*
[b] *Laboratoire Roberval, FRE 2012 CNRS, Alliance Sorbonne Université, Université de Technologie de Compiègne, Centre de recherche Royallieu, CS60319, 60203, Compiègne Cedex, France*
[c] *Institute of Mechanics, Materials and Civil Engineering, UCLouvain, 1348 Louvain-la-Neuve, Belgium*

Abstract

This study proposes a surrogate-based optimization model of the external patch design for damaged carbon fiber reinforced polymer (CFRP) laminates to improve the impact-resistance. Initially, finite element (FE) models of patch-repaired CFRP laminates constructed using continuum damage mechanics (CDM) approach and cohesive zone model (CZM), those well capture the intra- and inter-laminar damages during the low-velocity impacts, respectively. Experimental measurements of low-velocity impact tests concur with the numerical predictions and validate the FE models. Subsequently, the validated models are used to optimize the design parameters of repair patch, consisting of patch radius, thickness and off-axis angle. The optimum design parameters are identified using the surrogate models which are constructed using Diffuse Approximation and Design of Experiments (DOE). The identified optimum patch configurations significantly enhance the impact-resistance of repaired CFRP laminates by decreasing the impact energy absorption and the delamination surface area. Finally, the robustness of the optimization model is confirmed via error analysis of surrogate model reconstruction, and testing the influence of polynomial basis and weighting functions.

Keywords: CFRP laminates, External patch repair, Optimization, Surrogate-based model, Impact resistance

1. Introduction

External patch repairs have been widely applied as a rapid and economic solution for the maintenance of composites [1–6], such as carbon fiber reinforced polymer (CFRP) laminates. Unfortunately, like any kind of composite structures, patch-repaired CFRP laminates present the high susceptibility to low-velocity impact damage caused by threats, including runway debris or dropped tools. Thus, the impact-resistance of patch-repaired CFRP laminates is crucial to evaluate their repair performance. There are many design parameters concerning the impact-resistance of

*Corresponding author.
Email address: yulianghou@zzu.edu.cn (Yuliang Hou)

the patch-repaired laminates [7–12], such as patch shape, size, thickness, stacking sequence etc. However, the correlation of these design parameters on the repair performance is highly complicated due to the presence of multiple variables. Thus, it requires a systematic optimization strategy to identify the optimum design parameters for manufacturing the patch-repaired composite structures with maximum impact-resistance.

Experimental and numerical investigations on the impact behaviors of patch-repaired composite structures revealed that the repair performance depends not only on the manufacturing process, but also on the external patch design [13–23]. In the study of Balaganesan et al. [18], the energy absorption and the impact damage of repaired glass/epoxy composite laminates were numerically and experimentally investigated for high-speed impacts at different locations. The repaired laminates absorbed only 50-80% of impact energy that the unrepaired one absorbed during the impact process, and exhibited significant increase of service life. Coelho et al. [19] studied multiple-impact behaviors of repaired composites using single and double patch designs. In their comparison, the double patch repair recovered the stiffness of the laminates close to the virgin one, and provided a better impact-resistance than the single patch repair. Andrew et al. [21] proposed super hybrid external patches using plain woven glass fabric and aluminium sheet to restore the impact-resistance of damaged glass/epoxy composite laminates. Further investigation of low-velocity impact and tension after impact (TAI) tests had been carried out on the repaired specimens to investigate the effect of hybridization and lay-up configuration of repair patch [22]. It was reported that the repaired specimens using the hybrid patches (i.e. outer layer of aluminum and inner layer of glass fiber), exhibited better impact-resistance than those conventionally repaired using homogeneous glass fiber patches.

Over the last two decades, various studies have been carried out to identify the optimized design for repair patch configuration using finite element (FE) methods [24–29]. Fekih et al. [25] developed a design of experiments (DOE) method to optimize the geometrical parameters of composite patches for a pre-cracked aluminum plate. Numerical simulations were performed for models with repair patches having 3^3 combinations of patch thickness, adhesive thickness and strength. A stress intensity factor (SIF) K was subsequently computed for each combination, and the optimal patch design was obtained via minimizing the value of K. In the study of Ramji et al. [26], a 3D FE simulation had been conducted to optimize the composite patch shape for an inclined center cracked panel, repaired by symmetrical patch. A reduction parameter of SIF was introduced to combine both mode I and mode II SIFs into one value, to evaluate the repair performance of the mixed-mode cracked panel. Moreover, they adopted a genetic algorithm based approach in-conjunction with FE analysis for the parameter optimization of patch geometry and adhesive thickness to obtain an excellent repair performance [27]. It was observed that the stress concentration was reduced by 80% in the specimen repaired with the optimum patch dimension and adhesive thickness.

In this study, a double symmetric patch repair is investigated experimentally and numerically to search for an optimal design of patch configuration to maximize the impact-resistance of repaired CFRP laminates. FE model used for the low-velocity impact simulation is established based on the continuum damage mechanics (CDM) [30, 31]. Firstly, the numerical model is validated using experimental tests prior to carry out an optimization process. Subsequently, a surrogate-based optimization protocol is adopted using 3D Latin Hypercube Sampling (LHS) [32] and Diffuse

Approximation [33, 34]. The optimization protocol enables to identify the optimal combination of multiple design parameters for the patch, including patch radius, off-axis angle and thickness. Then, the obtained optimal configurations are substituted into FE models to investigate the effect on the repair performance. Based on the FE simulations, the impact behaviors of the repaired CFRP laminates with the optimum patch configuration are compared with the unrepaired and repaired ones with non-optimum patch configuration. And, this investigation reveals the improvement in repair performance of optimized patches and additional insights into the impact-resistance of patch-repaired CFRP laminates.

2. Numerical modeling method

In this study, a CDM based approach is used to predict the fiber breakage and matrix cracking (intralaminar damage), while cohesive zone model (CZM) is used to capture the delamination and debonding (interlaminar damage) within the patch-repaired CFRP laminates [30, 31]. Further details of these composite damage models can be found in our previous studies [23, 29].

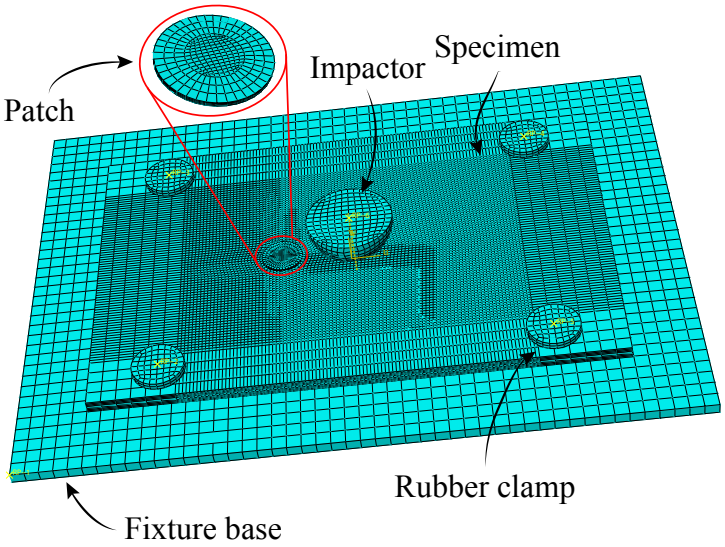

Figure 1: 3D FE model used for the low-velocity impact test showing the configuration with meshed geometries: specimen repaired with circular patches on double sides, impactor and clamping fixture.

Numerical simulations were performed to investigate the effect of various patch design parameters on the repair performance for CFRP laminates. Hence, 3D FE model was constructed to perform low-velocity impact simulation within Abaqus/Explicit framework [35], as illustrated in Fig. 1. The conventional solid elements with reduced integration (element type: C3D8R) and zero-thickness cohesive elements (element type: COH3D8) [35] were used to mesh the damaged laminates and double composite patches. Cohesive elements with non-zero thickness were placed between the parent laminates and repair patches to capture the damage behavior of the bondlines. To ensure the computational accuracy, element sizes of 1 mm and 5 mm (respectively for the refined and coarse mesh regions in Fig. 1) were adopted for various zones of the damaged laminates, while 0.5 mm and 1 mm were used for the repair patch. In addition, the patch-repaired specimen

was held by four rubber clamps (Fig. 1) during the whole simulation. Those cylindrical rubber clamps were meshed with solid element (element type: C3D8R) [35], and all their degrees of freedom (DOFs) were fixed. A hemispherical impactor having an initial velocity in the out-of-plane direction was assigned according to the experimental conditions, and it was also modeled with solid elements.

The numerical predictions from the simulation with the corresponding repair patch configuration of the experimental case, are compared with the measurements to validate the numerical model. Subsequently, an optimization procedure considering various design parameters, is performed using the numerical predictions to identify the optimum repair patch configuration (Section 4.1).

3. Experimental procedure and validation of the numerical model

3.1. Materials and specimen preparation

CFRP laminates T300/7901, with the dimension of 150 mm × 100 mm × 3.6 mm, were considered as the parent plates. It has the stacking sequence of $[(0_3/90_3)_2]_S$, and the density of 1478 kg/m^3. Other mechanical properties of the used CFRP laminates are obtained from in-house experiments, as listed in Table 1.

Table 1: Mechanical properties of the used CFRP laminates (T300/7901).

Elastic properties		**Damage properties**	
Intralaminar damage			
Young's modulus, E_1 (GPa)	125	Longitudinal tensile strength, X_T (MPa)	2000
Young's modulus, E_2, E_3 (GPa)	11.3	Longitudinal compressive strength, X_C (MPa)	1100
Shear modulus, G_{12}, G_{13} (GPa)	5.43	Transverse tensile strength, Y_T (MPa)	80
Shear modulus, G_{23} (GPa)	3.979	Transverse compressive strength, Y_C (MPa)	280
Poisson's ratio υ_{12}, υ_{13}	0.3	Shear strength, S (MPa)	120
Poisson's ratio υ_{23}	0.42	Fracture toughness fiber tension, G^t_{IC} (N/mm)	180
		Fracture toughness fiber compression, G^c_{IC} (N/mm)	100
		Fracture toughness matrix tension, G^t_{IIC} (N/mm)	4
		Fracture toughness matrix compression, G^c_{IIC} (N/mm)	10
Interlaminar damage			
Interface stiffness, K_{nn} (N/mm^3)	10^5	Maximum normal traction, t_n^{max} (MPa)	50
Interface stiffness, K_{ss}, K_{tt} (N/mm^3)	10^5	Maximum shear traction, t_s^{max}, t_t^{max} (MPa)	90
		Critical energy release rate mode I, G^I_C (kJ/m^2)	0.52
		Critical energy release rate mode II, III, G^{II}_C, G^{III}_C (kJ/m^2)	0.92

Geometrical specifications of the parent laminates and the repaired specimen are illustrated in Fig. 2. Circular holes with the radius of r = 3 mm were waterjet-cut on the CFRP laminates, and they were considered as the damage zones during the repair. The distance from the center of the hole to the center of the laminates was 20 mm in longitudinal direction while the impact was set for the center of the laminates. A double external patch design (manufactured from the same CFRP laminates with different stacking sequence of [0/90/0]) was used to repair the holes. Patches were prepared with two different shapes: (i) circular and (ii) octagon, as illustrated in

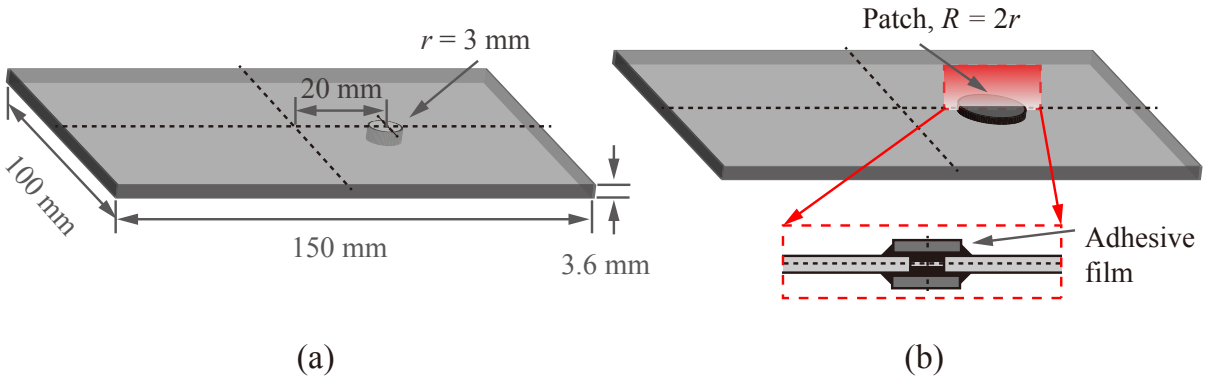

Figure 2: Schematic illustration showing the geometrical specifications: (a) damaged CFRP laminates and (b) specimen repaired with circular patches on the top and bottom sides.

Table 2: Mechanical properties of the adhesive film LJM-200.

Elastic properties		**Damage properties**	
Interlaminar damage			
Interface stiffness, K_{nn} (N/mm^3)	10^5	Maximum normal traction, t_n^{max} (MPa)	85
Interface stiffness, K_{ss}, K_{tt} (N/mm^3)	10^5	Maximum shear traction, t_s^{max}, t_t^{max} (MPa)	146
		Critical energy release rate mode I, G_C^I (kJ/m^2)	0.52
		Critical energy release rate mode II, III, G_C^{II}, G_C^{III} (kJ/m^2)	1.002

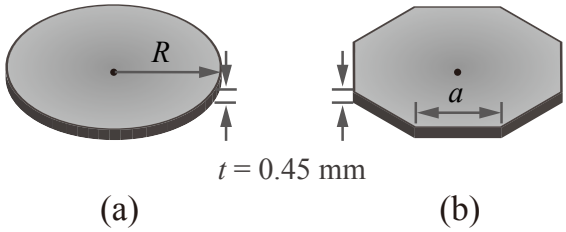

Figure 3: Geometry of: (a) circular and (b) octagon patches used in the experimental test plan.

Fig. 3 (for illustrative purpose Fig. 2b only includes the circular patches). In the test plan, the circular patch (Fig. 3a) was manufactured with the radius of $2r$ (6 mm). Moreover, the octagon patch was prepared with the side length of a = 4.84 mm (see Fig. 3b), which makes the patch area equal to the circular one. Adhesive film LJM-200 was used to bond patches and parent laminates, and its thickness is 0.12 mm. Mechanical properties of the used adhesive film are listed in Table 2. Patches were symmetrically bonded on both sides of the damaged laminates. This can effectively avoid the additional bending load and closely resemble to the actual repaired structures in engineering applications.

3.2. Low-velocity impact test

A low-velocity impact test system, including a hemispherical impactor, a specimen fixture, a data acquisition device and an anti-secondary impact device, was set up according to the ASTM D7136/D7136-15 standard, as shown in Fig. 4. The impactor with a radius of 12.5 mm and a mass

of 2.5 kg was used to perform the low-velocity impact test. The impactor was placed at a height of 0.54 m from the specimen, and it was attached with a dynamic force sensor (ICP 208C05) having the maximum capacity of 34 kN to record the impact force during the test (Fig. 4a). Beneath the impactor, the anti-secondary impact device (Fig. 4b) was placed to avoid the rebound of the impactor. The flat support fixture with a 125 mm × 75 mm rectangular cut-out allows the impactor to collide the specimen without interference. Before the low-velocity impact, repaired specimens were fastened on the support fixture with four rubber clamps (Fig. 4c). After the impactor was released with no initial speed, the impactor hit on the center of the repaired specimen with the velocity of 3.25 m/s and the impact energy of 13.2 J.

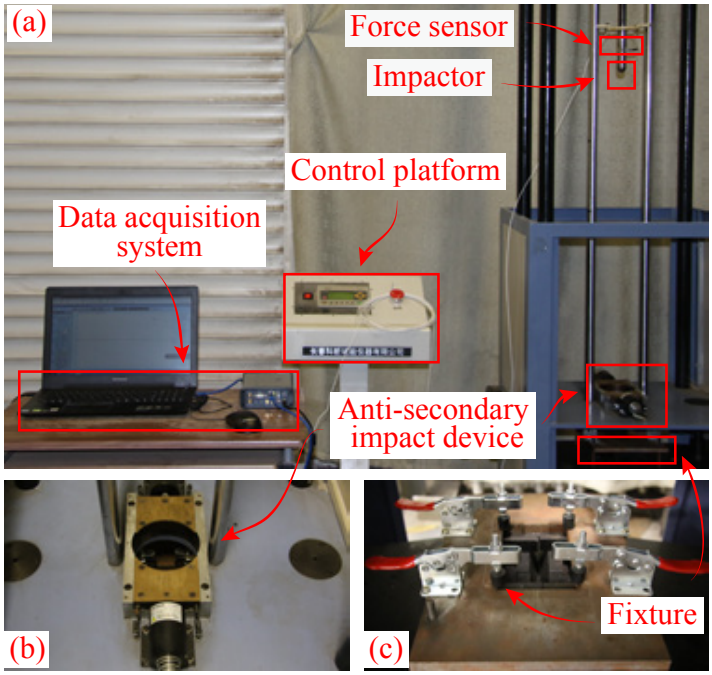

Figure 4: Illustration of: (a) experimental setup of the low-velocity impact test system (b) anti-secondary impact device and (c) specimen fixture.

During the low-velocity impact test, the data acquisition system recorded the instantaneous impact force using the dynamic force sensor. To ensure the reproducibility of the experimental measurement, three tests were performed for each configuration of the patch-repaired specimen. In each test, the onset of impact was identified by the sudden increase of impact force from the force history curves, and the peak impact force was reached before the impactor penetrates into the specimen. And then, the transient velocity $v(t)$ and kinematic energy $E_k(t)$ of impactor, the impact energy absorbed by the specimen $E_a(t)$ and the final damage dissipation energy $E_D(t)$ were calculated using the flow diagram given in Fig. 5. m is the mass of the impactor, $F(t)$ is the measured impact force, v_0 and $v(t)$ denote the initial and instantaneous velocities of the impactor, respectively. E_{k0} is the initial kinematic energy, and $E_e(t)$ represents the elastic energy of the specimen caused by the low-velocity impact. The damage surface area and absorbed energy were also measured for those patch-repaired CFRP laminates.

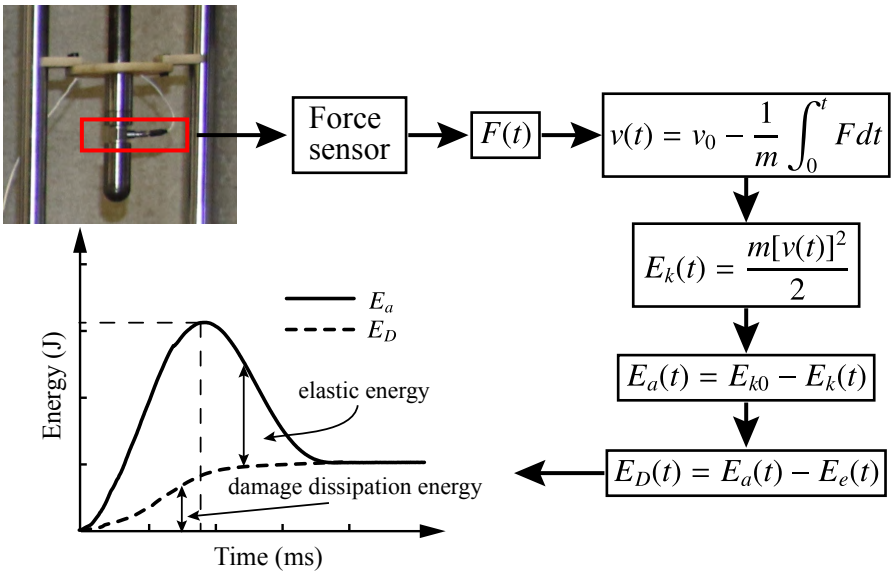

Figure 5: Flow chart explaining the computation steps for the impact energy using the measured impact force during the low-velocity impact test.

3.3. Experimental validation of the numerical model

Numerical simulations of low-velocity impact test were performed on the specimens repaired with the same patch configurations in the experimental plan, as presented in Section 3.1. The predicted results are compared with the experimental ones to validate the numerical modeling strategy. Correspondingly, the predicted and experimental history curves of impact force and absorbed impact energy are shown in Figs. 6 and 7, respectively.

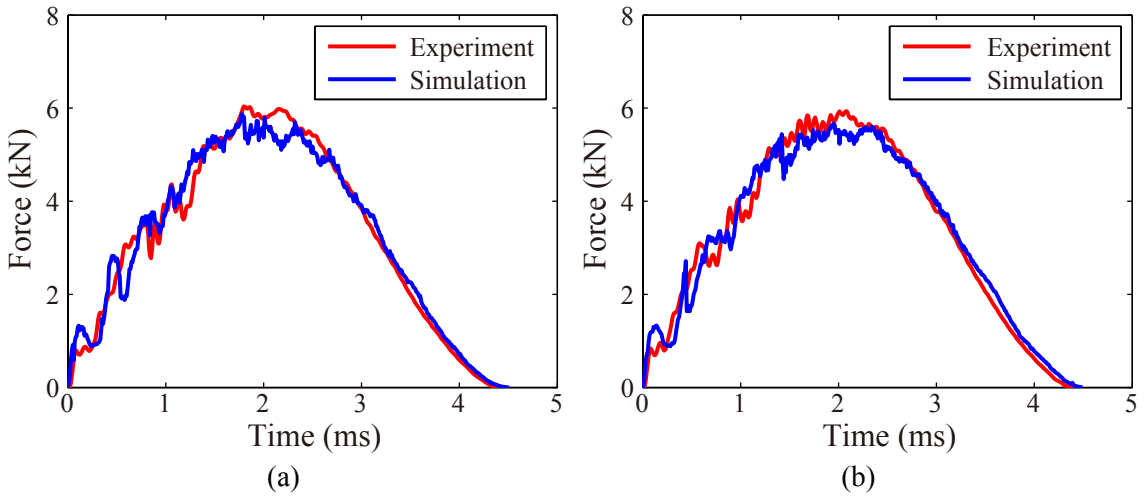

Figure 6: Comparison of impact force curves between predicted and experimental results for low-velocity impact tests on the specimens repaired with (a) circular and (b) octagon double patches.

Slight dissimilarities are observed in the comparison of impact force as shown in Fig. 6. In the case where the circular patch configuration is used, the maximum values of impact force are

6.022 kN and 5.871 kN with respect to the experimental and numerical tests. Whilst, these values are 5.936 kN and 5.641 kN for the specimen repaired with octagon patches, respectively. The force peaks almost appear at the same time in the history curves. The relative errors between the experimental and numerical results are 2.51% and 4.97% for the circular and octagon patches, respectively. Moreover, the history curves of absorbed impact energy in Fig. 7 show that, there exists no noticeable difference between simulation and experiment for the maximum and final impact energy absorbed by the repaired specimens. Hence, it clearly indicates that, the predicted results are in a good agreement with the experimental ones in both comparisons.

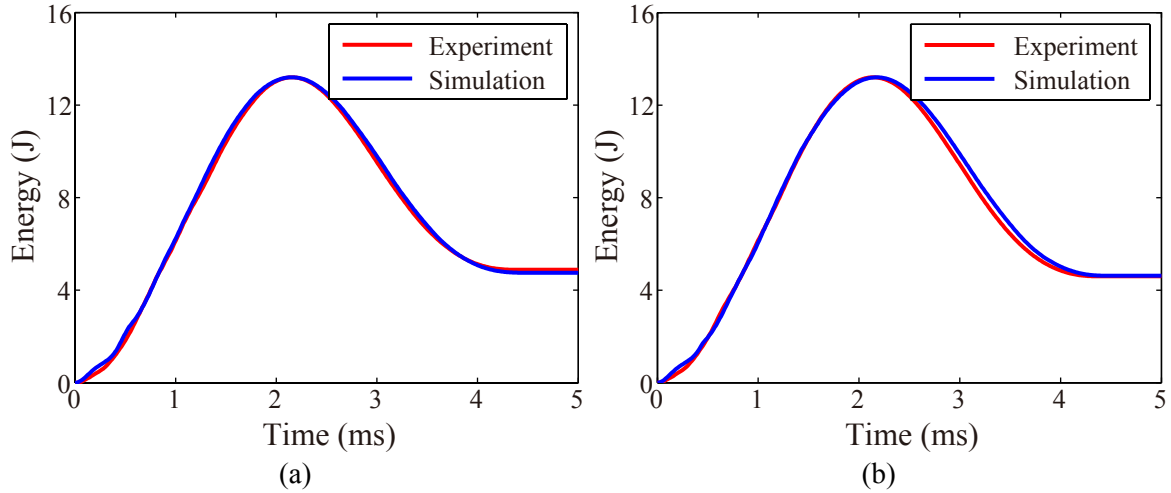

Figure 7: Comparison of absorbed impact energy curves between predicted and experimental results for low-velocity impact tests on the specimens repaired with (a) circular and (b) octagon double patches.

Table 3: Delamination surface areas of repaired specimens after low-velocity impact from experimental tests and numerical simulations for both circular and octagon double patches.

Specimen	Experiment (mm^2)	Simulation (mm^2)	Relative error
Circular patch	621	664	6.92%
Octagon patch	717	690	3.36%

Additionally, the delamination surface areas on repaired specimens caused by low-velocity impacts are also compared to further examine the reliability of the numerical model, as listed in Table 3. The delamination surface of each experimental case has been captured for both the top (impacted side) and bottom sides. Since the bottom side clearly shows the delamination surface, the relevant area has been measured from each specimen's bottom side. The delamination surface areas are approximately 621 mm^2 and 717 mm^2 for the specimens repaired with circular and octagon double patches, respectively. Furthermore, the deleted cohesive elements associated with the delamination surface of each case have been calculated from the numerical predictions. Accordingly, the simulations provide the delamination areas corresponding to circular and octagon patches equal to 664 mm^2 and 690 mm^2, respectively. There exist the relative errors of 6.92% and 3.36% between the experimental and numerical results in these two cases. It indicates that the

predicted delamination areas closely resemble the experimental ones. Together with the impact responses (history curves of impact force and absorbed energy), the reliability of the numerical modeling strategy is confirmed. Therefore, this robust model is adopted to perform the optimization study of the repair patch configuration.

4. Optimization for repair patch configuration

In general, the shape and size of a patch significantly affect the impact-resistance, the growth of patch separation and the final damage mode of patch-repaired composite structures. Moreover, the repair performance of composite patch has an obvious sensitivity to the patch thickness and layup configuration [23, 29]. Therefore, these parameters are selected as the design variables to search for the optimized configuration of repair patch to maximize the impact-resistance of repaired structure. The optimization is carried out using a surrogate-based model, which is constructed using Diffuse Approximation. The following section focuses on the description of the used optimization model for the repair patch configuration.

4.1. Optimization model for the design of repair patch

In our previous study [23], it was identified that the composite patch with circular shape possesses the capability to provide a better performance than others for single external repair patch. In addition, the experimental and numerical results in Section 3.3 support this conclusion; i.e. the specimen repaired with circular patches exhibits a higher impact-resistance than that repaired with octagon ones, in terms of absorbed energy and delamination surface area. This result is attributed to the distribution of impact load which is more even at the vicinity of the damage hole when using a circular patch, and it leads to a lower stress concentration during the impact. Hence, the circular patch is considered as the pre-defined shape to search for other optimal design parameters.

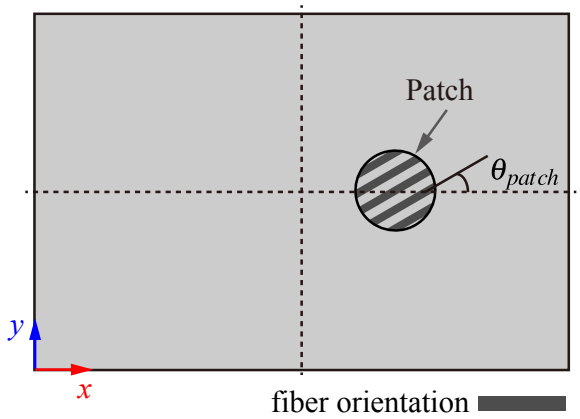

Figure 8: Illustration showing the definition for the off-axis angle between the fiber orientation of the patch and the longitudinal direction (along positive x axis) of parent laminates.

On the premise, the circular shape is chosen while its area mainly depends on the radius R. Moreover, a parameter which takes into account the fiber orientation within the patch, is proposed to simplify the design variable associated to the layup configuration. Before introducing this parameter, it is assumed that, all the constituent plies of composite patch orient in the same direction.

And, the angle between the fiber orientation of patch and the longitudinal direction (x direction) of parent laminates is defined as the patch off-axis angle θ_{patch}, as illustrated in Fig. 8. Together with the patch thickness t, there are totally 3 unknown parameters (R, θ_{patch}, t) to be identified.

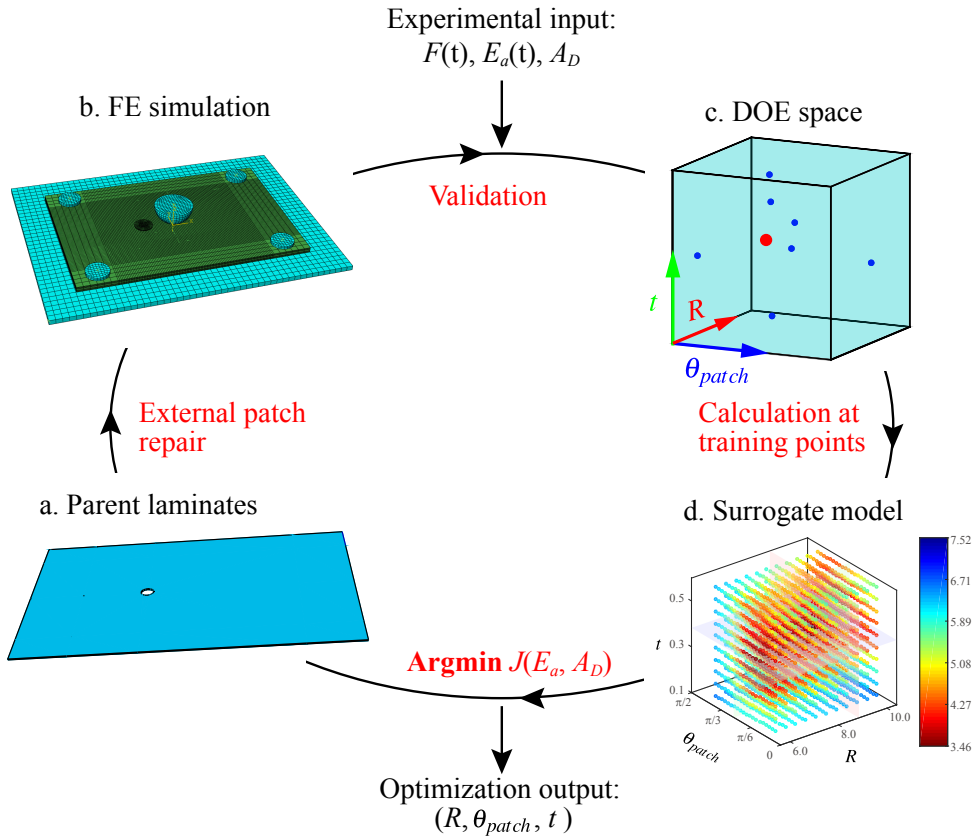

Figure 9: Flow chart showing the construction procedure of surrogate-based optimization model for the patch-repaired CFRP laminates.

To construct the surrogate model, experimental training points of target parameters (R, θ_{patch}, t) are selected using LHS approach from the DOE space, which corresponds to a reasonable range of each parameter according to experience-driven heuristics. Based on the aforementioned numerical modeling approach, low-velocity impact simulations have been performed on patch-repaired specimens, in which the patch configuration is set corresponding to these training points. An optimization indicator $J(E_a, A_D)$ is proposed to evaluate the combination of the final impact energy absorbed by repaired specimen (E_a) and the delamination area caused by the low-velocity impact (A_D). The surrogate model of the optimization indicator (J) is constructed using Diffuse Approximation [32]. Fig. 9 illustrates the surrogate-based optimization model used to identify the optimum patch configuration to maximize the impact-resistance of repaired CFRP laminates. In summary, the procedure consists of the following steps:

i. Parent plates with damage hole (Fig. 9a) are repaired using external double patches with given design configurations;
ii. Experimental and numerical tests of low-velocity impact are performed on these repaired specimens to record the corresponding impact responses and damage behaviors (Fig. 9b).

History curves of impact force $F(t)$, absorbed energy $E_a(t)$ and the delamination area A_D, obtained from experimental results, are used to validate the numerical model;

iii. Initial guess of target parameters (R^0, θ^0_{patch}, t^0) are used as the center (red dot in Fig. 9c) to create the DOE space for the construction of surrogate model. Subsequently, a number of low-velocity impact simulations are performed on repaired laminates with the external patches corresponding to each training point within the DOE space (blue dots in Fig. 9c);

iv. The final absorbed energy E_a and the delamination area A_D of each training point are obtained from the numerical simulation. The predictions related to E_a and A_D for the whole DOE space is computed using Diffuse Approximation. Surrogate models of E_a and A_D (Fig. 9d) are respectively reconstructed to identify the optimal target parameters by minimizing their values;

v. The optimal patch configuration design allowing to maximize the impact-resistance of repaired structure is determined using the objective function given by:

$$\textbf{Argmin}\, J(E_a, A_D) = \alpha \cdot E_a + \beta \cdot A_D \tag{1}$$

where α and β are weighting coefficients referred to E_a and A_D, respectively.

According to our previous study [23], as patch radius increasing, the energy absorbed by different repaired specimens remains the same, while there exists a significant dissimilarity for the delamination areas. The difference is caused by the different penetration depths of the impactor into the repaired specimens when using different patch radii. Hence, a valid evaluation of impact-resistance corresponding to each repaired specimen should consider the resistance in both in-plane and out-of-plane directions. Therefore, the optimization indicator $J(E_a, A_D)$, which combines these two forms of impact-resistances, is proposed in this study. Furthermore, the proposed surrogate-based optimization model not only ensures the effectiveness of the optimization process, but also significantly reduces the experimental and computational costs. Further details of the surrogate model are given in the following section.

4.2. Surrogate model based on Diffuse Approximation

According to the optimization procedure presented in Fig. 9, a 3D target parameter DOE including K points is designed and expressed by matrix $\mathbf{P} = [\mathbf{R}, \boldsymbol{\theta}_{patch}, \mathbf{t}] = [\mathbf{p}^1, \mathbf{p}^2, \mathbf{p}^3, \ldots, \mathbf{p}^K]^T$. Let $\mathbf{E}_a(\mathbf{P})$ and $\mathbf{A}_D(\mathbf{P})$ respectively denote the vectors of the final absorbed energy and delamination area at those training points within the DOE space. The surrogate model of E_a and A_D for the whole DOE space is constructed using Diffuse Approximation [32]:

$$\tilde{\mathbf{E}}_a(\mathbf{P}) = \mathbf{b}(\mathbf{P})^T \cdot \mathbf{a}(\mathbf{P}) \tag{2}$$

and

$$\tilde{\mathbf{A}}_D(\mathbf{P}) = \mathbf{b}(\mathbf{P})^T \cdot \hat{\mathbf{a}}(\mathbf{P}) \tag{3}$$

where $\mathbf{b} = [b_1, b_2, \ldots]^T$ refers to the polynomial basis vector. For a three-dimensional case, the polynomial basis vector can be expressed in terms of the target parameters:

$$\mathbf{b} = [1, R, \theta_{patch}, t, \ldots]^T \tag{4}$$

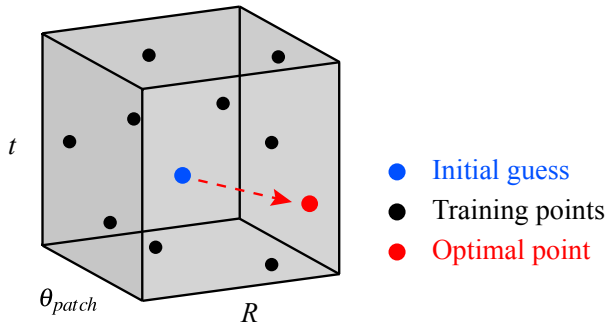

Figure 10: 3D DOE design associated with target parameters (R, θ_{patch}, t) using LHS approach.

In these two cases, the vectors of coefficients $\mathbf{a} = [a_1, a_2, \dots]^T$ and $\hat{\mathbf{a}} = [\hat{a}_1, \hat{a}_2, \dots]^T$ are the minimizers of functions defined by:

$$\Phi(\mathbf{a}) = \frac{1}{2}\sum_{k=1}^{K} w(\|\mathbf{p} - \mathbf{p}^k\|)(\mathbf{b}^T\mathbf{a} - \mathbf{E}_a(\mathbf{p}^k))^2 \tag{5}$$

$$\Phi(\hat{\mathbf{a}}) = \frac{1}{2}\sum_{k=1}^{K} w(\|\mathbf{p} - \mathbf{p}^k\|)(\mathbf{b}^T\hat{\mathbf{a}} - \mathbf{A}_D(\mathbf{p}^k))^2 \tag{6}$$

where $w(\|\mathbf{p} - \mathbf{p}^k\|)$ is the Gaussian weighting function, whose value mainly depends on the Euclidean distance d between the approximated point $\mathbf{p}$ and the training point $\mathbf{p}^k$:

$$w(\|\mathbf{p} - \mathbf{p}^k\|) = e^{-(\frac{d}{h})^2} \tag{7}$$

and h denotes a fixed parameter reflecting the anticipated spacing between the training points. The application of this parameter can be used to smooth small fluctuation in the data [36].

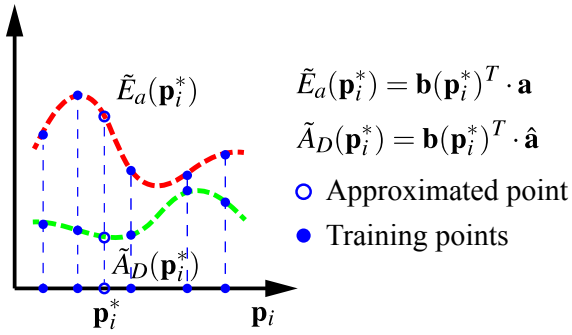

Figure 11: Illustration of the Diffuse Approximation procedure used to estimate the values of E_a and A_D at point $\mathbf{p}_i^*$ using the results at training points within DOE design.

During the implementation of the optimization procedure, the 3D DOE space, including a limited number of training points, is initially proposed using the initial guess and LHS scheme, as shown in Fig. 10. The design variables corresponding to each training point $\mathbf{p}_i$, are used as the configuration of circular patch to repair parent laminates. And then, numerical simulations of low-

velocity impact are performed on these repaired specimens, and the relevant damaged behaviors are predicted accordingly. For a given set of estimations for $\tilde{E}_a$ and $\tilde{A}_D$ at the approximated point $\mathbf{p}_i^*$, Fig. 11 schematically illustrates the approximation procedure based on the numerical predictions at the training points $\mathbf{p}_i$ (blue dots in Fig. 11). Furthermore, the approximated values for the whole design space are locally interpolated using Diffuse Approximation. Then, the surrogate models of E_a and A_D are constructed using Eqs. (5) and (6). A set of optimal parameters (red dot in Fig. 10) are identified by minimizing the surrogate model of $J(E_a, A_D)$, for a certain group of α and β.

Through this reduced-order method, the surrogate model of $J(E_a, A_D)$ is constructed with only a limited number of computations at the training points. Moreover, the complex nonlinear interaction between the design variables and the impact-resistance related to the repaired specimen is effectively captured using the surrogate models, as presented in Section 5.1.

5. Results and discussion

5.1. Surrogate models for optimization of repair patch configuration

The optimization methodologies proposed in the previous section are employed to identify the target parameters (R, θ_{patch}, t) of repair patch configuration for maximizing the impact-resistance of repaired specimen. Initially, a quadric polynomial basis (2nd-order), consisting of 10 terms, is used to construct the surrogate models in Eqs. (2) and (3). Within a reasonable design space Ω: $\Omega = \{R \in [6, 10.5]$ mm, $\theta_{patch} \in [0, \pi/2]$ and $t \in [0.15, 0.60]$ mm$\}$, 11 training points are chosen via LHS approach, as listed in Table 4. Results associated with impact-resistance are obtained from numerical simulations of low-velocity impact at these training points. Predictions of E_a and A_D are approximated for the whole DOE space. Subsequently, the approximation of $J(E_a, A_D)$ is computed using Eq. (1) within the whole DOE space. Moreover, a set of optimal parameters is obtained for each surrogate model and presented in the following sections.

Table 4: Results obtained from numerical simulations of low-velocity impact at the training points.

Training point	R (mm)	θ_{patch} (rad)	t (mm)	E_a (J)	A_D (mm^2)
1	8.686	0.568	0.297	4.173	649
2	6.069	0.816	0.237	4.725	741
3	9.542	0.197	0.414	4.279	666
4	6.937	0.913	0.460	4.458	692
5	10.069	0.275	0.354	3.629	645
6	7.807	0.674	0.573	4.682	698
7	8.950	0.936	0.530	4.302	703
8	7.332	0.546	0.506	3.874	670
9	8.250	$\pi/2$	0.375	4.703	687
10	6.687	1.398	0.152	4.302	731
11	10.243	1.253	0.278	4.043	638

5.1.1. *Surrogate model of E_a*

According to FE simulations at those training points listed in Table 4, the surrogate model of E_a has been constructed using Diffuse Approximation. Since the DOE space is three-dimensional in this case, the corresponding surrogate model becomes a four-dimensional data cluster. In order to present the surrogate model, a color spectrum consisting of different values of E_a is assigned to the data cluster, as shown in Fig. 12a.

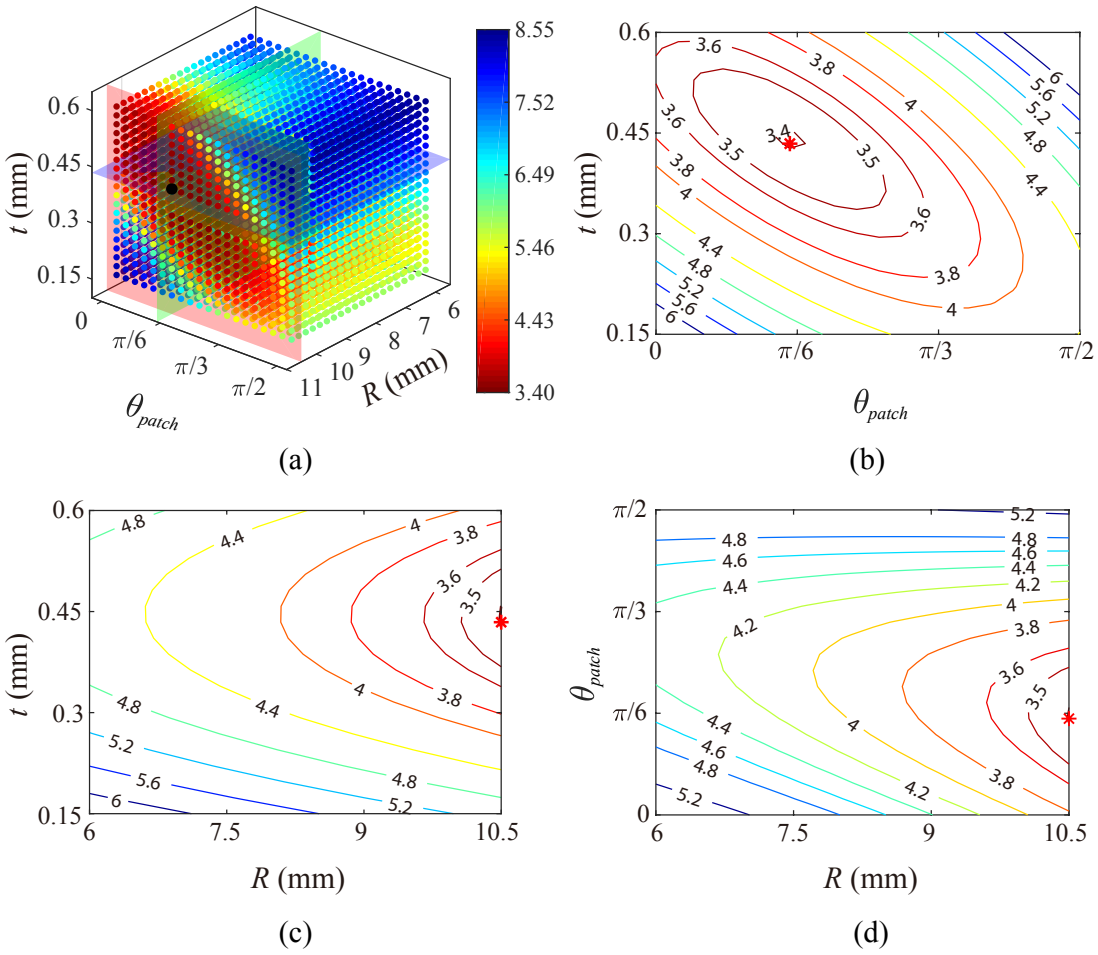

Figure 12: Surrogate model of E_a (denoted by the color scale) constructed using Diffuse Approximation (a) in (R, θ_{patch}, t) space, and the projected contours of E_a on various parameter planes of: (b), (θ_{patch}, t), (c), (R, t) and (d), (R, θ_{patch}). Those orthogonal profiles highlighted with transparent red, green and blue colors in (a) represent the planes of R = 10.5 mm, θ_{patch} = 0.496 and t = 0.434 mm, respectively. Black dot in surrogate model (a) and red stars in contour plots (b)-(d) denote the optimum solution.

In the data matrix, a black dot corresponding to the minimum value of E_a = 3.395 J, has been identified as the optimal solution, (10.5 mm, 0.496, 0.434 mm). Obviously, this optimal solution falls on the plane of R = 10.5 mm (the cross profile with transparent red color in Fig. 12a). It is attributed to the absorbed energy which decreases nonlinearly with the increase of patch radius. Furthermore, the circular patch with larger radius provides a better repair performance for single patch-repaired CFRP laminates, and it is also in good agreement with the earlier study [23]. As

the range of design parameter R is limited to 10.5 mm, the optimal value of the patch radius just overlaps at the boundary of the design space.

In order to intuitively illustrate the tendency of E_a within the whole design space, contours are projected on the orthogonal planes, as given in Figs. 12b-d. Red stars in these contours (corresponding to the black dot in Fig. 12a) denote the optimal solution identified by minimizing the surrogate model of E_a. In the contour projected on plane of (θ_{patch}, t) (Fig. 12b), the optimal solution is located at the point of ($\pi/6$, 0.45 mm), which is inside the tested ranges of θ_{patch} and t. The value of E_a increases when both design parameters (θ_{patch} and t) move away from this identified point. And, the distribution of the surrounding isolines exhibits a series of concentric ellipses, whose short axis denotes either the direction of the steepest descent or ascent. Likewise, the isolines in the two other contours (Figs. 12c and d) also reveal the shape of concentric ellipses. However, the optimal solution is located on the upper boundary of the proposed range of R in both cases. Moreover, the distribution of the isolines indicates that, E_a could be further reduced to a smaller value along with the increase of the upper boundary of R.

5.1.2. Surrogate model of A_D

Based on the numerical predictions of training points listed in Table 4, the surrogate model of A_D is constructed for the whole design space, as shown in Fig. 13a. The minimum value of A_D is identified as 622 mm^2, while having the optimal solution of (10.5 mm, 0.827, 0.150mm) denoted by the black dot in the data cluster (Fig. 13a).

Compared with the surrogate model of E_a, the optimal solution of A_D is located on the boundaries of R and t. That is, the patch with maximum radius and minimum thickness is identified for providing better repair performance regarding to the delamination area caused by the low-velocity impact. Likewise, contours projected on the various parameter planes from the surrogate model of A_D, are shown in Fig. 13b-d. In these contours, red stars denote the optimal solution (corresponding to the black dot in Fig. 13a). From the contours projected on planes of (θ_{patch}, t) and (R, θ_{patch}) (Figs. 13b and d), the optimal solution is located in the midst of the varying range of θ_{patch}. When θ_{patch} comes to 0.827, the minimum delamination area is caused on the corresponding patch-repaired specimen. However, according to the contour projected on the plane of (R, t) (Fig. 13c), the optimal solution falls on the maximum and minimum boundaries of R and t, respectively. Moreover, the delamination area A_D increases with the decrease of the patch radius and the increase of patch thickness within the whole design space.

In the earlier study with single patch repair, the smallest patch configuration with single layer absorbed the highest energy and exhibited the largest delamination areas after the low-velocity impact [29]. It is different from the results presented here for the double-patch case. This is primarily attributed to the change of patch number and the relative location during the repair. In the single patch case, only a circular patch was bonded on the top side of the damaged specimen (the impacted side), the local strength and impact-resistance are mainly recovered owing to the repairment. However, the restored properties of the bottom side are relatively weaker than that of the top side. Furthermore, delamination initiates and propagates along the bottom side. Hence, the recovery due to the patch repair on the top side provides limited improvement to the resistance to delamination on the bottom side. In other words, the resistance to delamination is more likely dependent on the patch repair performed at the bottom side of damaged specimen. It requires

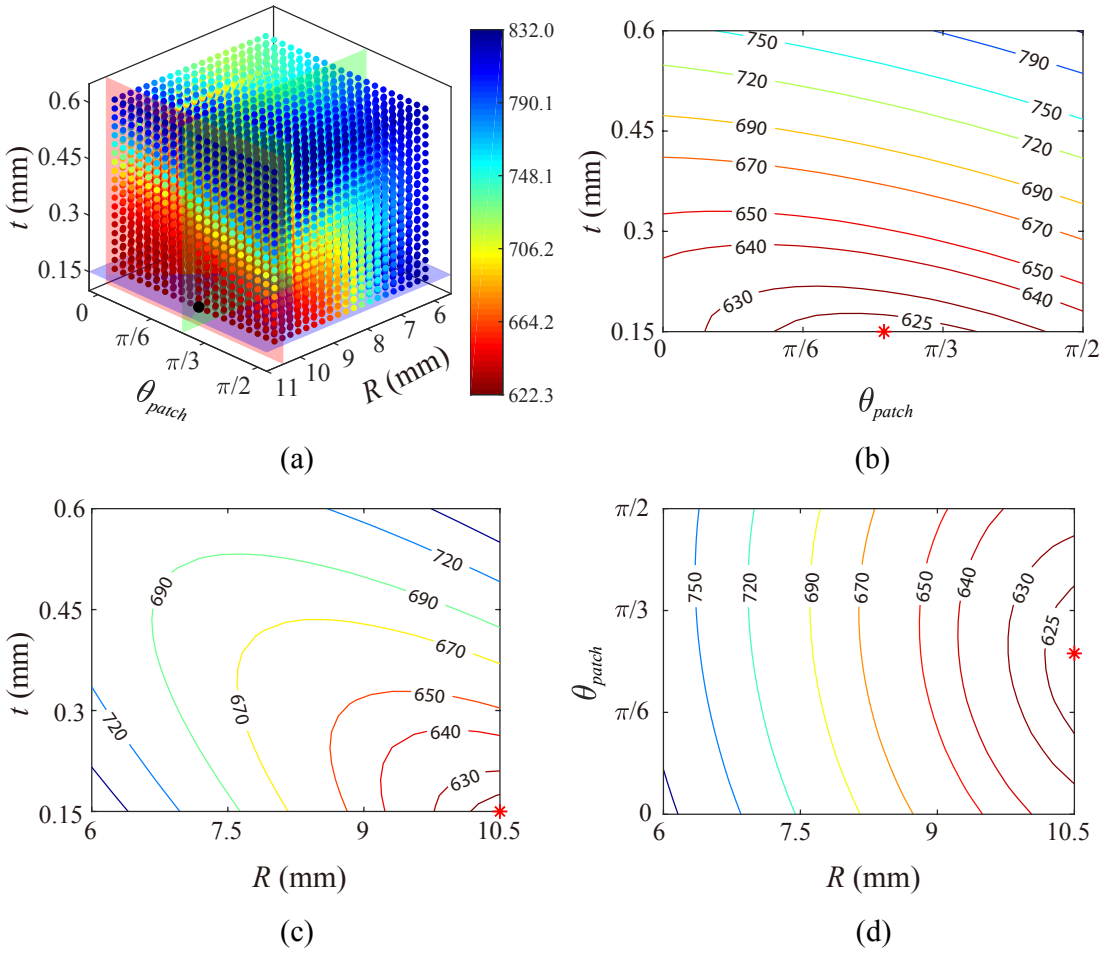

Figure 13: Surrogate model of A_D (denoted by the color scale) constructed using Diffuse Approximation (a) in (R, θ_{patch}, t) space, and the projected contours of A_D on various parameter planes of: (b), (θ_{patch}, t), (c), (R, t) and (d), (R, θ_{patch}). Those orthogonal profiles highlighted with transparent red, green and blue colors in (a) represent the planes of R = 10.5 mm, θ_{patch} = 0.827 and t = 0.15 mm, respectively. Black dot in surrogate model (a) and red stars in contour plots (b)-(d) denote the optimum solution.

further experimental and numerical investigations to validate this observation.

5.1.3. Surrogate model of $J(E_a, A_D)$

In the present study, a normalization-based approach is proposed to determine the weighting coefficients α and β, taking into account both the damage dissipation energy E_a and delamination area A_D during the patch optimization process. The weighting coefficients are normalized by the maximum values obtained from the surrogate models of E_a and A_D, given by:

$$\alpha = \frac{a}{\tilde{E}_a^{max}} \tag{8}$$

$$\beta = \frac{b}{\tilde{A}_D^{max}} \tag{9}$$

where a and b are the importance factors associated with E_a and A_D, respectively. And, their values are defined as 2/3 and 1/3 in this study, and further discussion about these importance factors is given in Section 5.2.3. $\tilde{E}_a^{max}$ and $\tilde{A}_D^{max}$ denote the maximum values extracted from the surrogate models of E_a and A_D, whose values are 8.55 J and 832 mm^2. Thus, the objective function given in Eq. (1) is transformed into:

$$\textbf{Argmin}\, J(E_a, A_D) = \frac{a}{\tilde{E}_a^{max}} \cdot E_a + \frac{b}{\tilde{A}_D^{max}} \cdot A_D \tag{10}$$

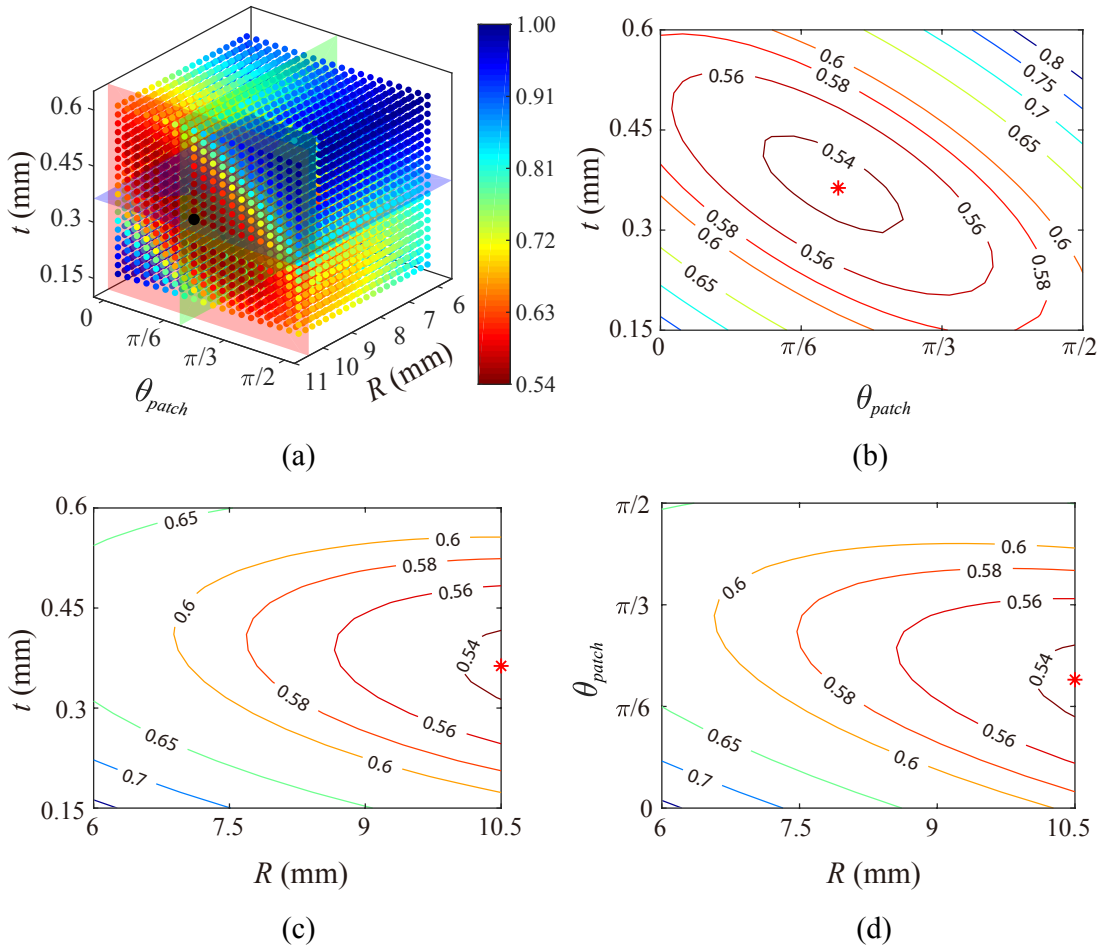

Figure 14: Surrogate model of J (denoted by the color scale) constructed using Diffuse Approximation (a) in (R, θ_{patch}, t) space, and the projected contours of J on various parameter planes: (b), (θ_{patch}, t), (c), (R, t) and (d), (R, θ_{patch}). Those orthogonal profiles highlighted with transparent red, green and blue colors represent the planes of R = 10.5 mm, θ_{patch} = 0.661 and t = 0.36 mm, respectively. Black dot in surrogate model (a) and red stars in contour plots (b)-(d) denote the optimum solution.

Based on the results obtained at the training points, the surrogate model of the proposed objective function J has been established using Diffuse Approximation, as shown in Fig. 14a. By minimizing the objective function, the optimal patch configuration is identified as (10.5 mm, 0.661,

0.36 mm). Similarly, a black dot which represents the minimum value of 0.535, is identified as the optimum solution in the data cluster (Fig. 14a). In this case, the optimal solution also emerges on the plane of $R = 10.5$ mm, which resembles the identified results from surrogate models of E_a and A_D.

In addition, Figs. 14b-d show the contours of J projected on parameter planes of (θ_{patch}, t), (R, t) and (R, θ_{patch}), respectively. Similar to the surrogate model of E_a, the optimal solution identified from the objective function J is also located approximately at the center of the varying range of θ_{patch} and t, as shown in Fig. 14b. The diffused distribution of isolines indicates that, the repair patch with the design configuration of $\theta_{patch} = \pi/5$ and $t = 0.36$ mm provides better recovery of impact-resistance, when R is equal to 10.5 mm. Furthermore, the optimal solution falls on the upper boundary of R within the contours of (R, t) and (R, θ_{patch}) as indicated in Figs. 14c and d. As the value of R increases, the objective function nonlinearly reduces from 0.70 to 0.54. It also supports that, an enhanced repair performance is achievable when using the patch design with the maximum radius in this design space.

5.2. Verification of robustness

5.2.1. Error analysis of surrogate model reconstruction

To further understand the optimization procedure, an error analysis is performed to quantify the influence of surrogate model reconstruction on the optimization criterion (Eq. (10)). For consistency, the relative error ε is computed with respect to a pseudo-target $\hat{J}(E_a, A_D)$ obtained from the surrogate model on a set of pre-defined points, given by:

$$\varepsilon = \frac{|J(E_a, A_D) - \hat{J}(E_a, A_D)|}{J(E_a, A_D)} \tag{11}$$

where $J(E_a, A_D)$ and $\hat{J}(E_a, A_D)$ denote the objective functions on each pre-defined point calculated from the numerical simulation and surrogate model, respectively. Hence, relative error of the objective functions on each pre-defined point is calculated from the corresponding low-velocity impact simulation and surrogate model, as listed in Table 5.

Table 5: Relative error of the objective functions for each pre-defined point calculated using the numerical simulation and surrogate model.

Pre-defined point	R (mm)	θ_{patch} (rad)	t (mm)	$J(E_a, A_D)$	$\hat{J}(E_a, A_D)$	ε
1	10.5	0.496	0.45	0.528	0.543	2.84%
2	10.5	0.827	0.15	0.567	0.595	4.94%
3	10.5	0.661	0.3	0.524	0.541	3.24%
4	6.0	0.0	0.15	0.954	0.988	4.61%
5	10.5	$\pi/2$	0.6	0.879	0.899	2.28%

As Table 5 indicates, acceptable errors are obtained (less than 5%) when comparing with the results obtained from the numerical simulation. These minor errors mainly resulted from the error during the surrogate model reconstruction. However, one must be noted that, the surrogate models are constructed using numerical results on the training points. Hence, the error induced by the used numerical modeling strategy is not considered in this error analysis.

5.2.2. Effect of polynomial basis

In this study, the surrogate models of E_a and A_D for the whole design space are constructed using a set of training points at the vicinities of current estimation point. Since it allows for a gradient and Hessian evaluation, a quadratic polynomial basis is used throughout the optimization process. Nevertheless, the number of coefficients of quadratic basis rises dramatically with the number of design parameters. Therefore, it is of necessity to investigate a lower order bilinear basis for the sake of reduction in the number of training calculations per optimization process. Especially, the lower order polynomial basis benefits to efficiently and prominently identify the optimal solution when more parameters are involved in the repair patch design. For instance, in a case where 5 parameters are involved, the quantities of training points per optimization process for bilinear and quadratic bases are 16 and 21, respectively.

Table 6: Results extracted from numerical simulations of low-velocity impact at training points using a bilinear basis.

Training point	R (mm)	θ_{patch} (rad)	t (mm)	E_a (J)	A_D (mm^2)
1	7.959	1.401	0.281	4.293	655
2	10.442	0.507	0.344	3.725	639
3	7.460	1.157	0.496	4.528	691
4	8.662	0.319	0.555	3.867	667
5	8.250	$\pi/2$	0.375	4.703	687
6	6.401	0.178	0.381	4.16	666
7	9.896	1.401	0.239	4.333	663

To investigate the effect of polynomial basis, a second optimization process including 7 training points, is performed using a bilinear basis to reconstruct the surrogate models of E_a and A_D, as reported in Table 6. Furthermore, the optimal solution of repair patch configuration is identified by minimizing the objective function given in Eq. (10).

Fig. 15a illustrates the surrogate model of the objective function J reconstructed using the bilinear basis and Diffuse Approximation. It reveals that the minimum value of J equal to 0.585, is identified at the point (10.5 mm, 0, 0.15 mm). Moreover, the optimal solution is located on a vertex of the DOE space, and it is different from that of the quadratic basis. The direct explanation of this dissimilarity is that the bilinear basis is used to reconstruct the surrogate model, whose projection on each parameter range exhibits pure linearity. Hence, peak (maximum and minimum) values definitely appear on the boundaries of each varying range.

Additionally, the error distribution (ε_J) between the surrogate models of J reconstructed using bilinear and quadratic bases is extracted to evaluate the reconstruction capacity of the used bilinear basis shown in Fig. 15b. Within the whole DOE space, the value of ε_J varies in the range of [-0.066, 0.242]. From the distribution of ε_J, it is found that, the bilinear basis exhibits high-accurate reconstruction capacity at the center of the DOE space, compared with the quadratic one. Furthermore, an average relative error ($\Delta\bar{\varepsilon}_J$) is employed to directly study the global deviation of the bilinear basis, given by:

$$\Delta\bar{\varepsilon}_J = \int_\Omega \Delta\varepsilon_J \mathrm{d}\Omega = \int_\Omega \frac{|\varepsilon_J|}{J^Q}\mathrm{d}\Omega = \int_\Omega \frac{|J^Q - J^B|}{J^Q}\mathrm{d}\Omega \tag{12}$$

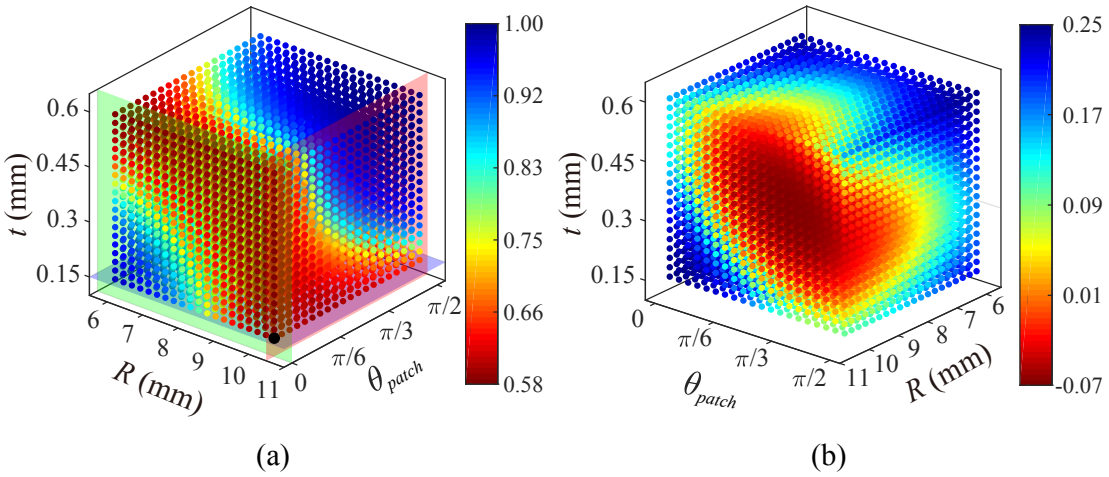

Figure 15: (a) Surrogate model of J (indicated by the color scale) reconstructed using the bilinear interpolation basis and Diffuse Approximation. Black dot in (a) represents the optimal solution, and the orthogonal profiles highlighted with transparent red, green and blue colors represent the planes of $R = 10.5$ mm, $\theta_{patch} = 0$ and $t = 0.15$ mm, respectively. (b) Error distribution (indicated by the color scale) between surrogate models of J reconstructed using bilinear and quadratic bases in (R, θ_{patch}, t) space.

where J^B and J^Q denote the J values extracted from the surrogate models reconstructed using bilinear and quadratic bases, respectively. Based on this integration formula, the value of $\Delta\bar{\varepsilon}_J$ is obtained as 6.59%. This global deviation is acceptable for an engineering optimization problem having multiple design parameters, especially the one with three or more design parameters.

5.2.3. Effect of α and β

In order to investigate the effect of the weighting coefficients on the optimization process, various values of α and β are used to deduce Eq. (10). And then, design parameters of repair patch configuration are identified for each re-defined objective function. Moreover, the variation of α and β is controlled via varying a and b, due to the correlation between weighting coeffients and importance factors, as given in Eqs. (8) and (9). Hence, as the importance factor a increasing from 0 to 1, the weighting coefficient α linearly rises from 0 to 0.117, and β decreases from 0.0012 to 0. The blue dots, green triangles and red diamonds in Fig. 16, respectively denote the optimal values identified for design parameters (R, θ_{patch}, t) by minimizing the corresponding objective function.

The blue dots in Fig. 16, indicate that the optimal value of R remains equal to 10.5 mm with the increase of a. Nonetheless, the optimal value of θ_{patch} (green triangles in Fig. 16) initially rises from 0.827 to 1.038 until the importance factor a comes to 0.135. Meanwhile, the optimal value of t (red diamonds in Fig. 16) is identified as 0.15 mm for a from 1 to 0.135. That is, the repair patch with 1 layer whose fiber orientation varies in the range of [0.827, 1.038], provides additional impact-resistance by reducing the delamination damage. After that, the optimal value of θ_{patch} decreases with an inapparent nonlinearity, and finally falls to 0.496 when $a = 1$. Concomitantly, the optimal value of t progressively increases to 0.434 mm. Therefore, concerning the impact energy dissipated by the patch-repaired laminates (as a increasing), the optimal configuration of repair patch is identified with more layers whose fiber orientation closes to the x-direction (the off-axial angle equals 0).

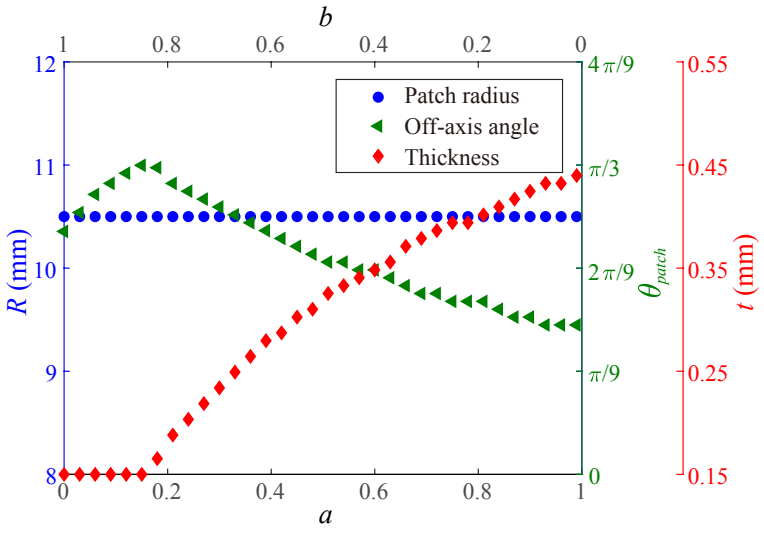

Figure 16: Optimal design parameters (R, θ_{patch}, t) identified using Eq. (10) and their variation along with the importance factors, a and b.

5.3. Repair performance of optimal external patch configuration

In this section, a comparison of the impact-resistance has been performed for the unrepaired and repaired specimens with non-optimal and optimal patch designs to evaluate the repair performance.

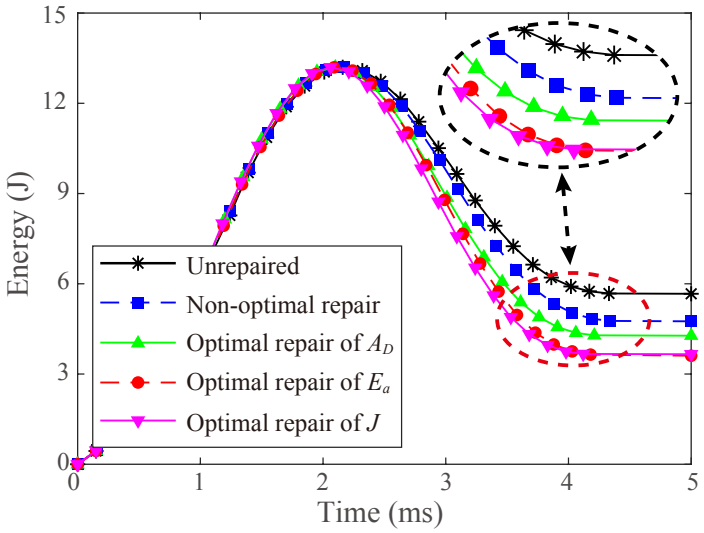

Figure 17: Predicted history curves of impact energy corresponding to the unrepaired and repaired specimens with non-optimal and optimal patch design configurations.

As presented in Section 5.1, three cases of patch configurations are identified as: (10.5 mm, 0.496, 0.434 mm), (10.5 mm, 0.827, 0.15 mm) and (10.5 mm, 0.661, 0.36 mm), using the surrogate models of E_a, A_D and J, respectively. Whereas, each layer within the repair patch possesses a given thickness (0.15 mm), so that the exact values of t should be an integer multiple of 0.15 mm.

Correspondingly, the thicknesses of these optimal patches are set as 0.45 mm, 0.15 mm and 0.3 mm, respectively. Moreover, the non-optimal patch design with circular shape presented in Section 3.1, is also used to compare the enhancement of repair performance induced by the optimized design. Numerical simulations of low-velocity impact have been performed for the unrepaired and repaired specimens with optimal and non-optimal patch designs to verify the optimization effect on the repair performance.

The predicted history curves of impact energy corresponding to unrepaired and repaired specimens with non-optimal and optimal patch designs are depicted in Fig. 17. It shows that, the unrepaired and repaired with specimen non-optimal patch design absorb 5.67 J and 4.75 J of total impact energy after the low-velocity impact. The non-optimal patch lowers the damage energy absorption of the damaged CFRP laminates by 16.2%. While, the repaired specimens absorb 3.61 J, 4.27 J and 3.69 J of impact energy, for the optimal patch designs identified using the surrogate models of E_a, A_D and J, respectively. It is found that, these optimal patch designs decrease the energy absorption by 36.3%, 24.7% and 34.9%, and improve the repair performance by 20.1%, 8.5% and 18.7% compared to the non-optimal patch design. This result clearly shows that the optimal patch designs based on the surrogate models of E_a and J provide better repair performance than that of the patch design based on the surrogate model of A_D.

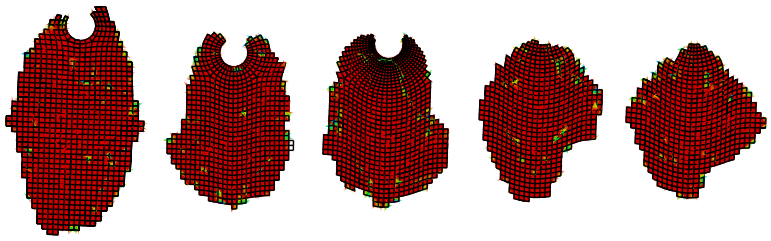

(a) (b) (c) (d) (e)

Figure 18: Predicted delamination surface areas of: (a) unrepaired specimen and repaired specimens with (b) non-optimal and optimal patch configurations obtained by minimizing (c) E_a, (d) A_D and (e) J, after low-velocity impact tests.

The delamination surface areas caused by the low-velocity impact has also been compared for the numerical simulations, as shown in Fig. 18. The delamination surface areas are approximately 783 mm^2 and 664 mm^2 for the unrepaired and non-optimal repaired specimens, respectively. Hence, the impact-resistance related to delamination damage is improved by 15.2% for the repaired specimen with non-optimal patch design. Moreover, by minimizing the sorrugate models of E_a, A_D and J, the delamination areas are reduced to 616 mm^2, 582 mm^2 and 596 mm^2 for the repaired specimens. The optimal patch designs based on the surrogate models of E_a, A_D and J, increase the impact-resistance of damaged CFRP laminates by 6.1%, 10.5% and 8.7% than the non-optimal patch design. The result shows that the optimal patch designs based on the surrogate models of A_D and J possess adequate repair capacity to minimize the delamination damage of composite laminates. Hence, by considering both impact energy absorption and delamination area, it is evident that the optimal patch based on the surrogate model of J exhibits the better repair performance. Therefore, the proposed surrogate-based model can achieve the optimized patch design for maximizing the impact-resistance of repaired CFRP laminates.

6. Conclusions

In this study, a surrogate-based model was proposed to optimize the repair patch design for maximizing the impact-resistance of repaired CFRP laminates. By employing design of experiment approach and Diffuse Approximation, surrogate models of various objective functions have been reconstructed using the numerical results at the training points. Optimal designs of patch configuration were identified using these surrogate models, and subsequently the repair performance of the identified configurations were investigated. The main contributions are listed as follows:

- A successful optimization model is implemented to seek for optimum patch design configurations using the proposed surrogate model by minimizing the impact energy absorbed by repaired specimen (E_a) and the delamination area caused by the low-velocity impact (A_D).
- A new objective function J considering both E_a and A_D was proposed combine the optimization procedure to seek an improved patch configuration that achieves an enhanced repair performance.
- Repair performance of optimal designs using surrogate-based model of J dramatically restores the impact-resistance of the damaged CFRP laminates, while decreasing the impact energy absorption and delamination area by 18.7% and 8.6% than the non-optimal design.
- Robustness of the surrogate-based model was confirmed using the error analysis of surrogated model reconstruction, the effect of polynomial basis and weighting coefficients. It is observed that, the proposed optimization scheme possesses the capacity to capture a systematic correlation of the design parameters.

Acknowledgements

Authors acknowledge the financial support from National Natural Science Foundation of China (No.U1833116), and the China Postdoctoral Science Foundation Funded Project (No.2018M6427-75). This study is also supported by Key Scientific Research Project of Colleges and Universities in Henan Province (No.20A460003). TS acknowledges F.R.S.-FNRS (Belgium) during his postdoc at UCLouvain.

References

[1] V. Rao, R. Singh, S. Malhotra, Residual strength and fatigue life assessment of composite patch repaired specimens, Composites Part B: Engineering 30 (6) (1999) 621–627.
[2] F. Z. Hu, C. Soutis, Strength prediction of patch-repaired CFRP laminates loaded in compression, Composites Science and Technology 60 (7) (2000) 1103–1114.
[3] H. Hosseini-Toudeshky, B. Mohammadi, H. R. Daghyani, Mixed-mode fracture analysis of aluminium repaired panels using composite patches, Composites Science and Technology 66 (2) (2006) 188–198.
[4] A. Ariaei, S. Ziaei-Rad, M. Ghayour, Repair of a cracked Timoshenko beam subjected to a moving mass using piezoelectric patches, International Journal of Mechanical Sciences 52 (8) (2010) 1074–1091.
[5] R. Moreira, M. De Moura, M. Figueiredo, R. Fernandes, J. Gonçalves, Characterisation of composite bonded single-strap repairs under fatigue loading, International Journal of Mechanical Sciences 103 (2015) 22–29.

[6] H. Chong, S. Liu, A. Subramanian, S. Ng, S. Tay, S. Wang, S. Feih, Out-of-autoclave scarf repair of interlayer toughened carbon fibre composites using double vacuum debulking of patch, Composites Part A: Applied Science and Manufacturing 107 (2018) 224–234.
[7] H. Park, C. Kong, A study on low velocity impact damage evaluation and repair technique of small aircraft composite structure, Composites Part A: Applied Science and Manufacturing 42 (9) (2011) 1179–1188.
[8] M. Kara, M. Uyaner, A. Avci, Repairing impact damaged fiber reinforced composite pipes by external wrapping with composite patches, Composite Structures 123 (2015) 1–8.
[9] Y. Xu, H. Lu, T. Gao, W. Zhang, Predicting the low-velocity impact behavior of polycarbonate: Influence of thermal history during injection molding, International Journal of Impact Engineering 86 (2015) 265–273.
[10] I. Ivañez, S. Garcia-Castillo, S. Sanchez-Saez, E. Barbero, Experimental study of the impact behavior of repaired thin laminates with double composite patch, Mechanics of Advanced Materials and Structures (2018) 1–8.
[11] X. Cheng, X. Du, J. Zhang, J. Zhang, X. Guo, J. Bao, Effects of stacking sequence and rotation angle of patch on low velocity impact performance of scarf repaired laminates, Composites Part B: Engineering 133 (2018) 78–85.
[12] B. Liu, Q. Han, X. Zhong, Z. Lu, The impact damage and residual load capacity of composite stepped bonding repairs and joints, Composites Part B: Engineering 158 (2019) 339–351.
[13] M. Charalambides, R. Hardouin, A. Kinloch, F. Matthews, Adhesively-bonded repairs to fibre-composite materials I. Experimental, Composites Part A: Applied Science and Manufacturing 29 (11) (1998) 1371–1381.
[14] M. Charalambides, A. Kinloch, F. Matthews, Adhesively-bonded repairs to fibre-composite materials II. Finite element modelling, Composites Part A: Applied Science and Manufacturing 29 (11) (1998) 1383–1396.
[15] P. Papanikos, K. Tserpes, G. Labeas, S. Pantelakis, Progressive damage modelling of bonded composite repairs, Theoretical and Applied Fracture Mechanics 43 (2) (2005) 189–198.
[16] H. S. Kim, M. Cho, J. Lee, A. Deheeger, M. Grédiac, J.-D. Mathias, Three dimensional stress analysis of a composite patch using stress functions, International Journal of Mechanical Sciences 52 (12) (2010) 1646–1659.
[17] J. Lee, M. Cho, H. S. Kim, Bending analysis of a laminated composite patch considering the free-edge effect using a stress-based equivalent single-layer composite model, International Journal of Mechanical Sciences 53 (8) (2011) 606–616.
[18] G. Balaganesan, V. C. Khan, Energy absorption of repaired composite laminates subjected to impact loading, Composites Part B: Engineering 98 (2016) 39–48.
[19] S. Coelho, P. Reis, J. Ferreira, A. Pereira, Effects of external patch configuration on repaired composite laminates subjected to multi-impacts, Composite Structures 168 (2017) 259–265.
[20] O. Balcı, O. Çoban, M. Ö. Bora, E. Akagündüz, E. B. Yalçin, Experimental investigation of single and repeated impacts for repaired honeycomb sandwich structures, Materials Science and Engineering: A 682 (2017) 23–30.
[21] J. J. Andrew, V. Arumugam, K. Saravanakumar, H. N. Dhakal, C. Santulli, Compression after impact strength of repaired GFRP composite laminates under repeated impact loading, Composite structures 133 (2015) 911–920.
[22] J. J. Andrew, S. M. Srinivasan, A. Arockiarajan, The role of adhesively bonded super hybrid external patches on the impact and post-impact response of repaired glass/epoxy composite laminates, Composite Structures 184 (2018) 848–859.
[23] Y. Tie, Y. Hou, C. Li, X. Zhou, T. Sapanathan, M. Rachik, An insight into the low-velocity impact behavior of patch-repaired CFRP laminates using numerical and experimental approaches, Composite Structures 190 (2018) 179–188.
[24] A. A. Yala, A. Megueni, Optimisation of composite patches repairs with the design of experiments method, Materials & Design 30 (1) (2009) 200–205.
[25] S. Fekih, A. Albedah, F. Benyahia, M. Belhouari, B. B. Bouiadjra, A. Miloudi, Optimisation of the sizes of bonded composite repair in aircraft structures, Materials & Design 41 (2012) 171–176.
[26] M. Ramji, R. Srilakshmi, M. B. Prakash, Towards optimization of patch shape on the performance of bonded composite repair using FEM, Composites Part B: Engineering 45 (1) (2013) 710–720.
[27] M. Kashfuddoja, M. Ramji, Design of optimum patch shape and size for bonded repair on damaged carbon fibre reinforced polymer panels, Materials & Design 54 (2014) 174–183.
[28] X.-J. Gong, P. Cheng, S. Aivazzadeh, X. Xiao, Design and optimization of bonded patch repairs of laminated composite structures, Composite Structures 123 (2015) 292–300.

[29] Y. Hou, Y. Tie, C. Li, T. Sapanathan, M. Rachik, Low-velocity impact behaviors of repaired CFRP laminates: Effect of impact location and external patch configurations, Composites Part B: Engineering 163 (2019) 669–680.
[30] G. Short, F. Guild, M. Pavier, The effect of delamination geometry on the compressive failure of composite laminates, Composites Science and Technology 61 (14) (2001) 2075–2086.
[31] M. Fakoor, S. M. N. Ghoreishi, Experimental and numerical investigation of progressive damage in composite laminates based on continuum damage mechanics, Polymer Testing 70 (2018) 533–543.
[32] Y. Hou, T. Sapanathan, A. Dumon, P. Culière, M. Rachik, A novel development of bi-level reduced surrogate model to predict ductile fracture behaviors, Engineering Fracture Mechanics 188 (2018) 232–249.
[33] L. Xia, B. Raghavan, P. Breitkopf, W. Zhang, Numerical material representation using proper orthogonal decomposition and diffuse approximation, Applied Mathematics and Computation 224 (2013) 450–462.
[34] L. Xia, P. Breitkopf, Multiscale structural topology optimization with an approximate constitutive model for local material microstructure, Computer Methods in Applied Mechanics and Engineering 286 (2015) 147–167.
[35] ABAQUS/Explicit: user's manual, Vol. 1, Hibbitt, Karlsson and Sorenson Incorporated, 2001.
[36] M. Alexa, J. Behr, D. Cohen-Or, S. Fleishman, D. Levin, C. T. Silva, Computing and rendering point set surfaces, IEEE Transactions on visualization and computer graphics 9 (1) (2003) 3–15.

A surrogate-based optimization model of repair patch design

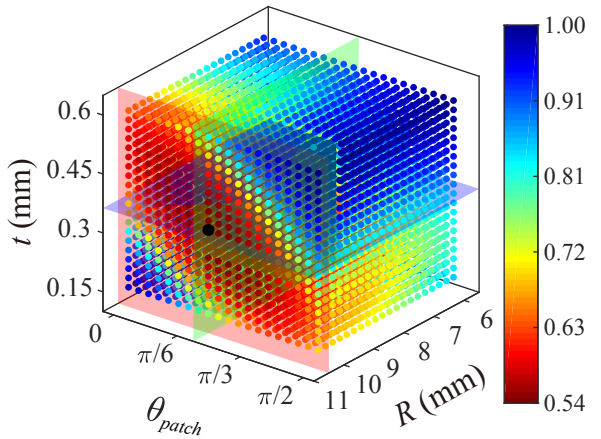

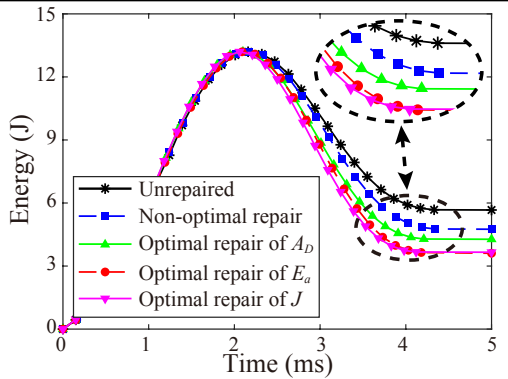

Impact energy absorption

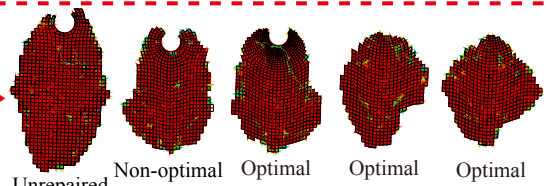

Delamination area